Materials Research Bulletin 153 (2022) 111914

Contents lists available at ScienceDirect

Materials Research Bulletin

journal homepage: www.elsevier.com/locate/matresbu

Research Papers

Effect of calcination temperature and pressure-assisted heat treatment on the dye degradation performance of SnO_2 photocatalyst obtained by a simple synthesis method

Letícia Guerreiro da Trindade [a,*], Ana Carolina Borba Rocha [b], Vinícius Teodoro [c], Vinicius Tineu da Silva [b], Aline Barrios Trench [c], Eloisa Cordoncillo [d], Marcio Daldin Teodoro [e], Sergio Mazurek Tebcherani [f], Elson Longo [c], Tatiana Martelli Mazzo [b,*]

[a] São Carlos Institute of Chemistry, University of São Paulo, São Carlos, SP 13560-970, Brazil
[b] Institute of Marine Science, Federal University of São Paulo, Santos, SP 11070-102, Brazil
[c] LIEC – CDMF - Department of Chemistry, Universidade Federal de São Carlos - UFSCar, P.O. Box 676, São Carlos, SP 13565-905, Brazil
[d] Departament de Química Inorgànica I Orgànica, Universitat Jaume I (UJI), Castelló de La Plana 12071, Spain
[e] Department of Physics, Federal University of São Carlos, São Carlos, SP 13565-905, Brazil
[f] Department of Production Engineering, Federal University of Technology – Paraná, Av. Monteiro Lobato km 04, Ponta Grossa, PR 84016-210, Brazil

ARTICLE INFO

Keywords:
SnO_2
Calcination
Pressure-assisted heat treatment
Photocatalytic activity

ABSTRACT

SnO_2 particles were synthesized by the co-precipitation method. The effect of annealing temperature and pressure-assisted heat treatment (PAHT) on their structural, morphological and optical properties were investigated. Moreover, the synthetized SnO_2 at ambient temperature and annealed at 400 and 700 °C as well as the particles submitted at the PAHT were efficient for the photocatalytic degradation of the Rhodamine B (RhB) dye solution under UV irradiation, showing a degradation efficiency above 99% for all samples studied. However, the SnO_2 sample obtained at ambient temperature (AT-SnO_2) exhibited complete RhB photodegradation in only 10 min. This surprising performance of the AT-SnO_2 sample led to the investigation of its performance for the degradation of two other dyes, methylene blue (MB) and methyl orange (MO), and the results also revealed complete degradation of these dyes. These findings were superior to those found in the literature for SnO_2 samples synthesized by different methods.

1. Introduction

Pollution through the inappropriate disposal of toxic organic dye residues in rivers caused by economic activities, especially the textile industry, can bring many consequences to human health, including some diseases such as cancer, besides posing a threat to aquatic life [1]. To overcome such disadvantages imposed by the industries, many methods to eliminate or degrade organic dye molecules from the effluents have been researched. In recent years, studies have focused on the use of semiconductor materials as photocatalysts for the degradation of these dyes. Generally, these photocatalysts are nanoparticles activated in the presence of visible or ultraviolet radiation [2]. Among the most used photocatalysts, TiO_2, ZnO and SnO_2 stand out due to their low cost, non-toxic nature and chemical stability [3].

SnO_2 is an n-type semiconductor material with a high band gap value (3.58 eV) [4] that has been widely studied for applications as gas sensors, energy storage devices, biomedical applications and dye-based solar cells among others [5–8]. However, since SnO_2 cannot effectively absorb visible solar light there are a few works in the literature addressing its use as a photocatalyst due to its wide band gap. Additionally, when irradiated by UV light, it can generate electron-hole pairs that produce radical species ($OH^{\cdot}$ and $O_2^{\cdot-}$) capable of decomposing most organic compounds [9].

Many synthesis methods and conditions have been used to obtain SnO_2 particles aiming at changes in their photocatalytic properties, such as morphology, crystal size, porosity, crystallinity, surface area, and so on [10,11].

Sadeghzadeh-Attar [12] synthesized SnO_2 nanotubes and calcined them at different temperatures (300–700 °C) for 1 h. These nanotubes (0.01 g) were tested for the degradation of methylene blue dye (MB)

* Corresponding authors.
E-mail addresses: lgt.gtrindade@gmail.com (L.G. da Trindade), tatiana.mazzo@unifesp.br (T.M. Mazzo).

https://doi.org/10.1016/j.materresbull.2022.111914
Received 25 September 2021; Received in revised form 28 April 2022; Accepted 25 May 2022
Available online 26 May 2022

Table 1
Sample designation and treatment.

Sample	Heat treatment (°C)	PAHT
AT-SnO_2	no	no
400 °C-SnO_2	400	no
700 °C-SnO_2	700	no
AT/HP-SnO_2	no	yes
400 °C/HP-SnO_2	400	yes
700 °C/HP-SnO_2	700	yes

(100 mL/10 mg L^{-1}) under UV irradiation. The results demonstrated that SnO_2 calcined at 600 °C showed higher photocatalytic activity (90.7%) in 180 min. This was attributed to the high crystalline nature and specific surface area of this material.

Li et al. [13] synthesized SnO_2 nanoparticles by the corrosion of metal Sn using concentrated nitric acid and tested them against the degradation of MB and RhB dyes under UV light irradiation. They observed that the degradation efficiency went from 90% to the complete degradation of the dyes under UV irradiation in 50 min (MB) and 270 min (RhB).

The purpose of this article was to synthesize SnO_2 particles by the co-precipitation technique using a simple, rapid and cost-effective method. Here, for the first time, the effects of annealing temperature and pressure-assisted heat treatment (PAHT) on their structure, morphology, and photocatalytic behavior were compared. The RhB aqueous solution was used to verify the photocatalytic activity under UV irradiation, and the RhB photocatalytic degradation kinetics and mechanism were investigated for all samples. Moreover, compared to other SnO_2 samples synthesized by different methods [14–19] for RhB degradation under UV light, the SnO_2 sample synthesized in this work by the co-precipitation method at room temperature showed a higher rate of degradation and better degradation efficiency in a short time interval when compared to other samples synthesized in the literature [14–19]. This superior performance of AT-SnO_2 regarding the RhB photocatalytic activity led us to investigate its performance for the degradation of two other dyes, methylene blue (MB) and methyl orange (MO).

2. Materials and methods

2.1. Synthesis of SnO_2

The SnO_2 samples were prepared by the co-precipitation (CP) method in aqueous media. A total of 6.77 g of $SnCl_2.2H_2O$ (Vetec) was added to 30 ml of H_2O under constant stirring. After total dissolution, 35 mL of H_2O_2 (31%, Synth) was added to the mixture. Finally, 35 mL of KOH solution (2 mol L^{-1}) (Synth) was added to promote the precipitation. The resulting precipitate was separated by centrifugation and washed with deionized water until reaching pH 7. Afterwards, the samples were oven-dried overnight at 70 °C and calcinated at 400 or 700 °C for 1 h at a heating rate of 20 °C min^{-1}.

2.2. Pressure-assisted heat treatment (PAHT)

The samples were submitted to PAHT according to the literature [20]. The procedure consists of heat treating the samples at 120 °C under an air pressure of 2 MPa for 48 h to evaluate the effect of PAHT on the dye degradation performance.

In this work we treated six samples, which were designated according to Table 1.

2.3. Characterization

The crystal phases of the SnO_2 samples were obtained by X-ray diffraction (XRD) (Rigaku, CuKα, $\lambda = 0.15406$ nm). The morphologies were analyzed by field emission scanning electron microscopy (FE-SEM) (ZEISS/105 DSM940A). Raman experiments were recorded at ambient temperature with a 532 nm laser source (JobinYvon T64000). Room temperature photoluminescence (PL) spectra were obtained using a 355 nm laser (Cobolt/Zouk) as excitation source, and the luminescence emitted by the samples was filtered and dispersed by a 19.3 cm spectrometer and detected by a Silicon CCD (Andor/Kimera -Idus). UV-visible diffuse reflectance spectra (Cary 5G/Varian) were performed and transformed into absorption spectra according to Tauc relation.

The AT-SnO_2 sample was analyzed by a transmission electron microscopy (TEM, FEI Tecnai F20) operating at 200 keV. Lastly, Brunauer-Emmett-Teller (BET, Micrometrics Tristar II 3020) analysis was performed for the AT-SnO_2, 400 °C-SnO_2 and 700 °C-SnO_2 samples.

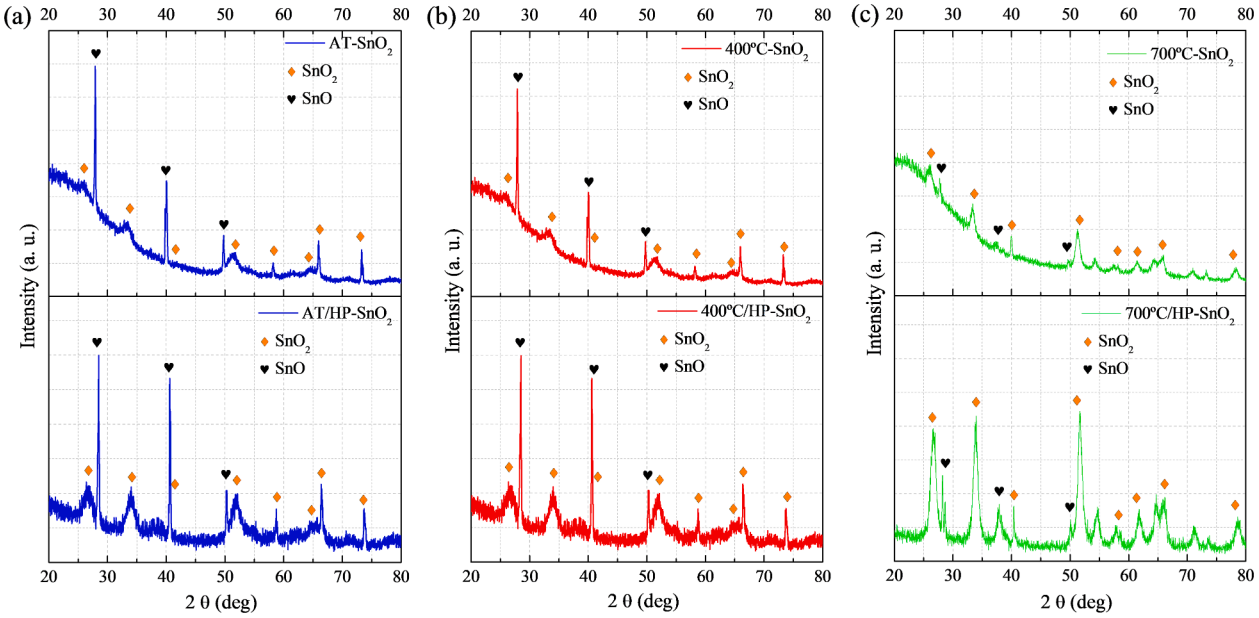

Fig. 1. XRD pattern of SnO_2 at ambient temperature (AT) (a), 400 (b), and 700 °C (c) under ambient pressure and pressure-assisted heat treatment (HP).

Table 2
Average particle size of SnO_2 annealing at different temperatures and subjected to PAHT from XRD and the lattice parameters calculated using Rietveld refinement.

Sample	Average size (nm)	Lattice constants (Å)		Volume (Å^3)
		a (=b)	c	
AT-SnO_2	10	4.7351	3.2549	72.98
400 °C-SnO_2	22	4.8442	3.2622	76.55
700 °C-SnO_2	38	4.7383	3.1859	71.53
AT/HP-SnO_2	84	4.7119	3.2278	71.66
400 °C/HP-SnO_2	162	4.8273	3.2521	75.78
700 °C/HP-SnO_2	209	4.7170	3.1732	70.60

2.4. Photocatalytic dye degradation performance

Photocatalytic activities of the samples were evaluated for Rhodamine B (RhB, 95%, Aldrich) degradation in aqueous solution (50 mL, 10 mg L^{-1}) under ultraviolet (UV) irradiation by six lamps (Osram, 15W). The selected sample (50 mg) was incorporated into the dye solution and then placed in ultrasonic bath (Branson 1510; 42 kHz) for 30 min. Previous to UV irradiation, the mixture was stirred for 30 min in the dark at a controlled temperature (20 °C) to establish the adsorption–desorption equilibrium between the photocatalyst and the dye. Subsequently, the mixture was irradiated, and aliquots (2 mL) were collected at different times and centrifuged to remove the photocatalyst powder. The RhB degradation was analyzed by measuring the absorbance at λ_{max} = 554 nm using an UV−vis spectrophotometer (V-660, JASCO).

Quenching experiments were carried out by adding tert-butyl alcohol (TBA, 0.1 mol L^{-1}), ammonium oxalate (AO, 1 10^{-3} mol L^{-1}), or benzoquinone (BQ, 1 10^{-3} mol L^{-1}) to the mixture, RhB and the best photocatalyst. TBA, AO and BQ are scavengers of the hydroxyl radical (OH·), hole (h^+) and superoxide radical (O_2^{-}), respectively. These reagents were supplied by Alfa Aesar.

3. Results and discussion

The X-ray diffraction (XRD) spectra of the SnO_2 samples are displayed in Fig. 1. It is clear that the samples at different calcination temperature are slightly crystalline with a great amorphous background. After increasing the calcination temperature and submitting the samples to pressure-assisted heat treatment, they show a more crystalline profile. The XRD pattern reveals the formation of SnO_2 phase for all samples, demonstrating rutile structure (JCPDS n°: 41-1445). Along with the SnO_2 phase, the formation of the secondary phase of SnO is also observed, which is in agreement with romarchite (JCPDS n°: 06-0395). All SnO_2 samples exhibit the (110), (101), (200), (211), (002), (310), (112) and (321) diffraction planes [21]. In contrast, the SnO secondary phase presents the (101), (002) and (112) planes [22]. This SnO phase is probably a minority phase resulting from the incomplete oxidation of Sn atoms. These results show that the calcination temperature and the PAHT greatly influence the crystallinity of the samples, leading to almost complete crystallinity at 700 °C under both conditions. SnO_2 is an oxide that does not densify, however, with the presence of SnO there is formation of oxygen vacancies, which facilitates densification. On the other hand, the association of temperature with pressure leads to better densification, due to the involvement with oxygen, which reacts with SnO to form SnO_2, increasing crystallinity.

The crystallite size was determined by the Scherrer Eq. (1) using the (110) and (111) diffraction planes [23]:

$$D_{XRD} = \frac{k\lambda}{\beta\cos\theta} \quad (1)$$

where k, λ, ß, and θ are the Scherrer constant, the X-ray wavelength (Cu-$K_{\alpha 1}$), the full width at half maximum of the diffraction peak (FWHM) and the diffraction angle, respectively.

The average crystallite size and the lattice parameters calculated by Rietveld refinement of all samples are listed in Table 2. According to the data, the crystallite size increases with increasing temperature and with the PAHT. However, these calculated average sizes of the particles may be different from the real size as there is a difficult to apply the peak-width based analysis to agglomerates since the small size and the mechanical stress in the clusters, lead to peak broadening [24]. As can be seen in Fig. 1, the increase in calcination temperature and pressure treatment make the peaks to be stronger and narrower. This behavior can be attributed to that at higher temperatures the particles grows larger and improves the degree of crystallinity [25]. The Rietveld refinement showed that the lattice constants a (=b) and c increase from 4.7351 Å and 3.2549 Å to 4.8442 Å and 3.2622 Å to the sample dry at 70 °C (AT-SnO_2) and the sample calcined at 400 °C (400 °C-SnO_2), respectively. This increase in the lattice parameters can be attributed to the water adsorbed on the crystallite surface of the AT-SnO_2 sample, since when the sample was annealed at 400 °C (400 °C-SnO_2) these adsorbed water molecules were eliminated from the SnO_2 surface thus increased the lattice constants [26]. Thereafter, for the sample annealing at 700 °C (700 °C-SnO_2) the lattice constants decreased (a (=b) = 4.7383 Å and c = 3.1859 Å). This reduction in the lattice constants with the annealing temperature can be attributed to the dehydroxylation of the samples, indicating the presence of large amount of the hydroxyl groups in the bulk of the SnO_2 crystallites, generating a bad crystallized rutile structure [26]. The volume variation of the unit cell follows this variation of the lattice parameters, increases when the sample is

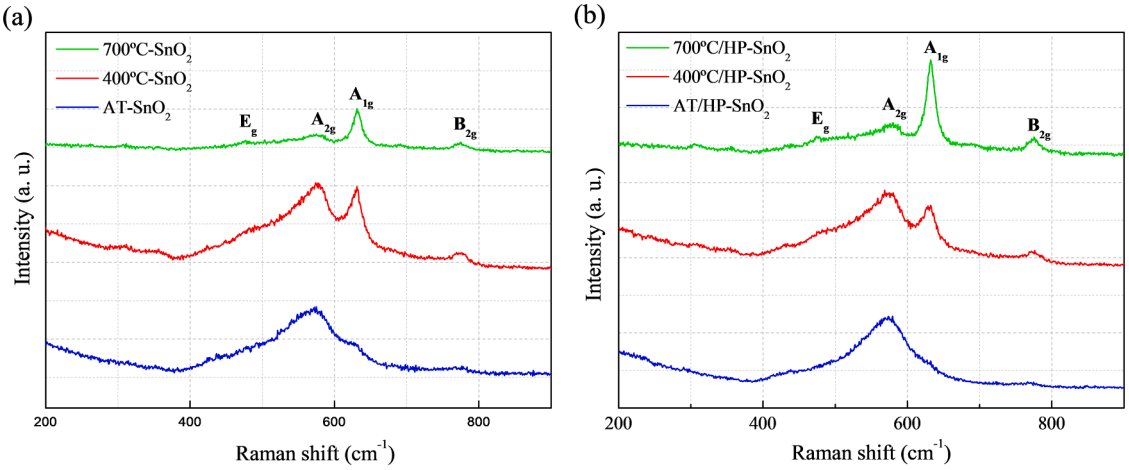

Fig. 2. Raman spectra of SnO_2 at ambient temperature (AT), 400 and 700 °C under ambient pressure and pressure-assisted heat treatment (HP).

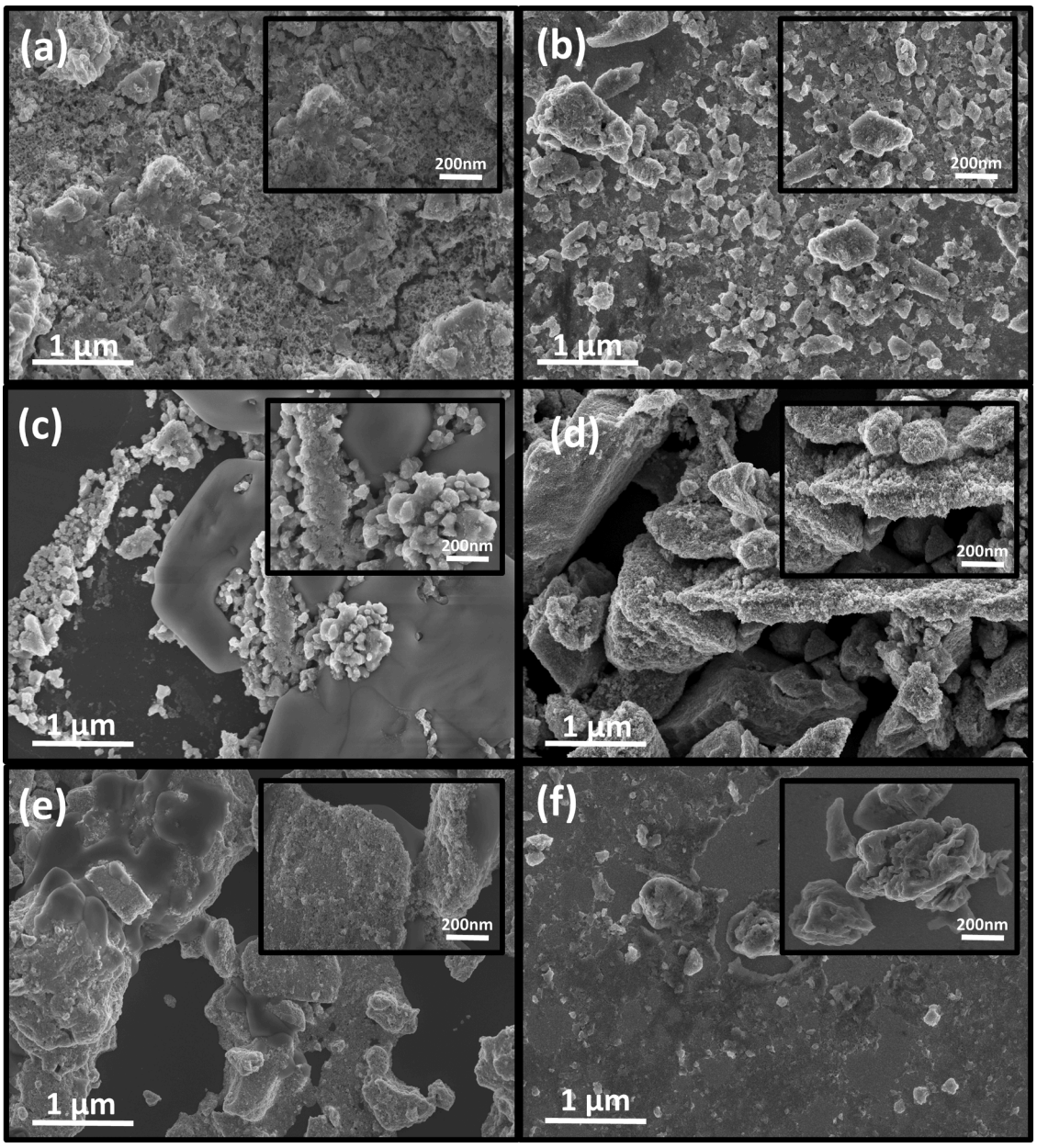

Fig. 3. FE-SEM of AT-SnO_2 (a), AT/HP-SnO_2 (b), 400 °C-SnO_2 (c), 400 °C/HP-SnO_2 (d), 700 °C-SnO_2 (e), and 700 °C/HP-SnO_2 (f).

annealed at 400 °C and decreases when the annealing temperature increases to 700 °C. This change in the values of lattice parameters and unit cell volume can be attributed to presence of oxygen vacancies and/or vacancies clusters, local lattice disorders and grain boundaries [27–32]. Compared to the samples submitted only to heat treatment, the samples submitted to PAHT showed a small contraction of lattice constants, and as a result, there is a reduction in the unit cell volume. It seems the decrease in lattice constants and unit cell volume to be related with the thermal stress and to PAHT.

Fig. 2 shows the Raman spectra of SnO_2 samples, where it is possible to see that the SnO_2 rutile structure presents the $1A_{1g}$, $1A_{2g}$, $2A_{2U}$, $1B_{1g}$, $1B_{2g}$, $2B_{1U}$, $1E_g$ and $4E_U$ lattice vibration modes [33]. It can also be noted that the number of lattice vibration Raman active modes increases as a function of the calcination temperature. All samples exhibit the A_{2g} and A_{1g} vibration modes, being the first related to the existence of oxygen vacancies in rutile SnO_2 [34]. The SnO_2 samples at 400 and 700 °C submitted or not to pressure-assisted heat treatment present a peak at 776 cm^{-1}, which corresponds to the B_{2g} mode. The A_{1g} and B_{2g} modes are related to the symmetric and asymmetric stretching of Sn-O bonds, respectively [35,36]. The E_g doubly degenerate mode arising from the vibration mode of oxide ions appears at 473 cm^{-1} for the samples calcinated at 700 °C. At 103 cm^{-1}, the Raman spectrum displays the E_{1g} mode, which can be attributed to SnO [37]. The absence of an intense and acute peak at 211 cm^{-1} (A_{1g}) indicates the absence of well-crystallized SnO formation [37]. These results corroborate the XRD data, evidencing that the calcination temperature and the pressure-assisted heat treatment influence the structural organization of the SnO_2 samples.

The FE-SEM images of all SnO_2 samples are shown in Fig. 3. It is possible to observe that the samples do not have a defined shape. Besides that, the heat and pressure treatments cause changes in their morphological profile. The AT-SnO_2 sample (Fig. 3a) exhibits aggregates composed of particles with varied grain sizes. It is clear that the heat treatment carried out at 400 and 700 °C (Fig. 3c and e) leads to the formation of small grains with smooth surface and dense packing. When all samples are subjected to PAHT (Fig. 3b, d and f), the particle

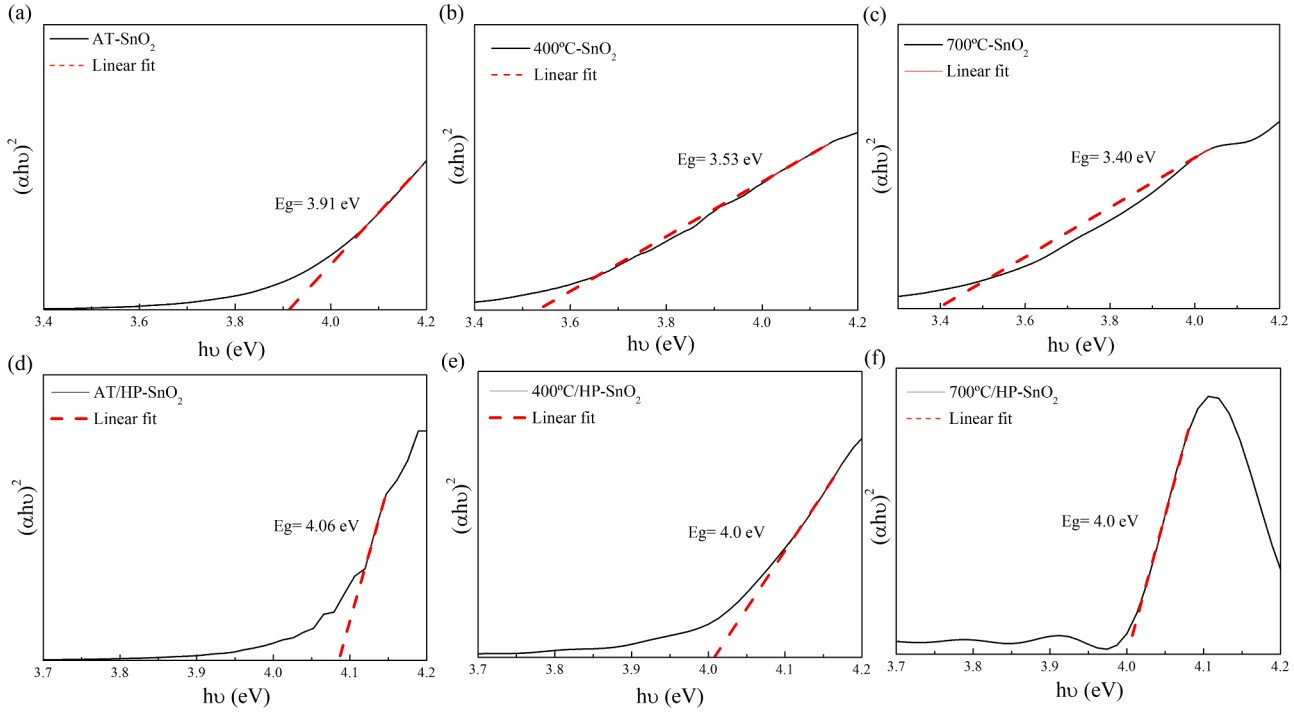

Fig. 4. Tauc plot of SnO_2 samples at different temperatures and under pressure-assisted heat treatment.

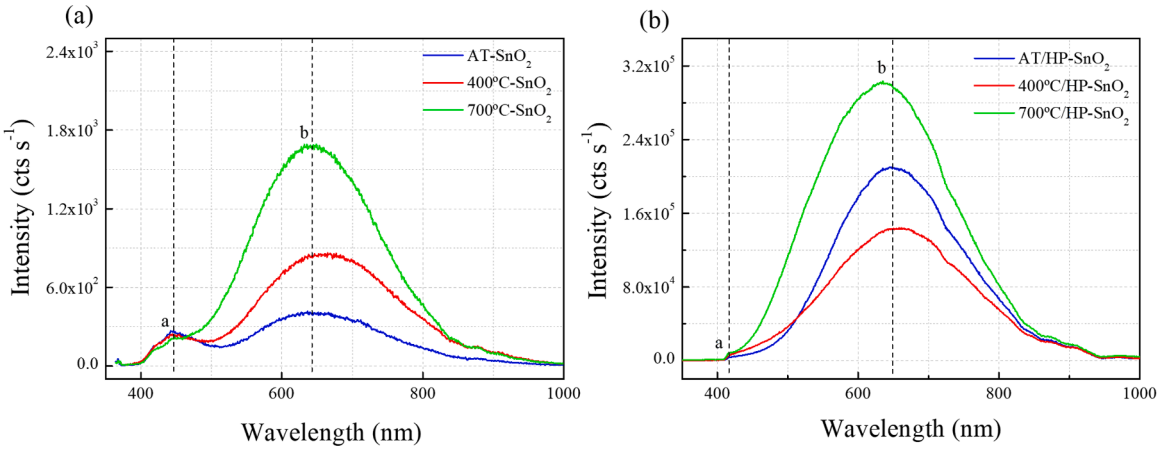

Fig. 5. PL spectra of SnO_2 at ambient temperature (AT), 400 °C and 700 °C under ambient pressure (a) and pressure-assisted heat treatment (b) with 355 nm excitation energy.

aggregates have their size increased as a function of temperature. In addition, the presence of smooth surface with dense packing cannot be observed.

The direct band gap values of the SnO_2 samples are shown in Fig. 4. The band gap energy (E_g) was obtained by UV-visible diffuse reflectance spectra and plotted $(\alpha h\nu)^2$ against photon energy ($h\nu$) using the Tauc method, according to Equation [38]:

$$(\alpha h\nu)^{1/\gamma} = B\left(h\nu - E_g\right), \quad (2)$$

where α is the absorption coefficient, h is the Planck constant, and ν and B are the photon frequency and constant, respectively. The γ factor value used was 1/2, which corresponds to direct transition band gaps.

It can be seen that the E_g values decrease from 3.91 to 3.40 eV with increasing the calcination temperature (Fig. 4a–c). In this typical semiconductor, the SnO_2 microcrystal lattice can have different types of characteristics in its electronic structure, such as intercluster (intermediary range) and intracluster (local range) interaction. The cluster-like elucidation of the order-disorder performance is supported and strengthened by different extrinsic (surface) and intrinsic (bulk) defect distributions. When the photons reach the surface, they may be trapped by extrinsic or intrinsic defects in the network modifier [SnO_6] complex clusters, inducing new energy in the band gap. The same trend is observed for the samples subjected to pressure treatment (Fig. 4d and e), that is, the values of E_g decrease with increasing the particle size. However, when the calcination temperature increases from 400 to 700 °C (Fig. 4f) the E_g value remains unchanged. In addition, it is possible to note that the pressure-assisted heat treatment causes an increase in the band gap value. These results indicate that the E_g values depend on the synthesis conditions, which in turn directly influence the size and surface of the particles, their optical properties, and consequently the penetration of photons of light [39].

Fig. 5 shows the photoluminescence (PL) spectra of all SnO_2 samples with 355 nm excitation energy. The spectra of SnO_2 at different

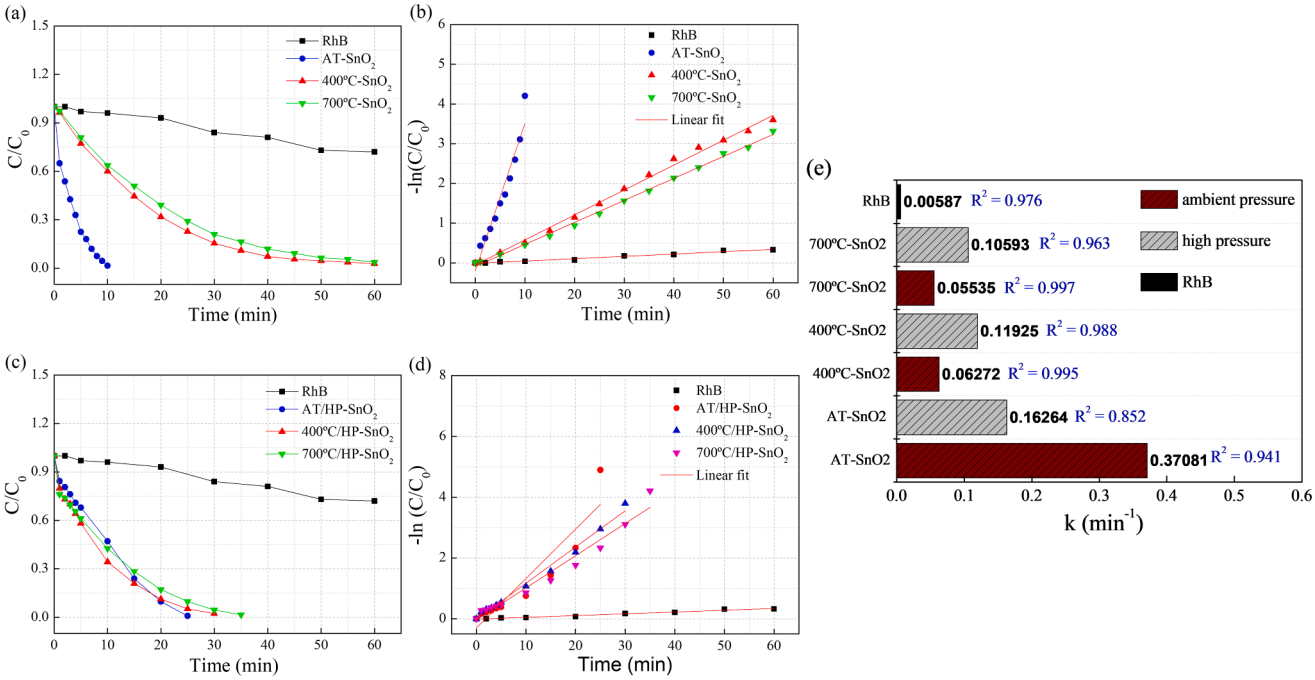

Fig. 6. Comparison among the photocatalytic RhB degradation of samples under UV light (a,c), the corresponding kinetic fitting (b,d) and reaction rate constants with the respective linear regression coefficient (R^2) (e).

temperatures and under ambient pressure can be split into two main peaks, according to Fig. 5a. The peaks at 445 nm and 642 nm can be attributed to the closest band-edge emission of SnO_2 and to oxygen vacancies, respectively [40,41]. The PL intensity of SnO_2 samples increases as a function of the calcination temperature, probably due to the decrease in the particle size along with an increase in the number of defects [42]. When these samples undergo pressure treatment (Fig. 5b), we can still observe the presence of the same two main peaks. However, peak (a) has its intensity reduced. There is also an increase in the PL intensity of 100 times compared to the samples synthesized at ambient pressure, which may be attributed to the larger particle size. This result is in agreement with the results obtained by XRD (Table 2) and by FE-SEM (Fig. 3) which show that when the samples are subjected to temperature and pressure treatments, the particles tend to have their size increased. This is in line with the Raman results (Fig. 2), which demonstrate that larger particles have better crystalline quality and fewer structural defects. The E_g values (Fig. 4) also corroborate this result, as there is a significant increase in the E_g values when these samples are submitted to pressure-assisted heat treatment. This behavior can be attributed to a reduction in intermediate levels, thus causing the electron-hole recombination to increase due to the decreased number of traps (defects), leading to a higher PL intensity. The sample calcined at 700 °C has higher PL intensity than the others at both pressures, pointing to an increase in the recombination rate of photo-induced charge carries [43]. The PL curve deconvolution of the samples using Gaussian analysis was discussed in detail in the supporting information (Fig. S1, SI).

Fig. 6 illustrates the effect of temperature and pressure treatments on the SnO_2 photocatalytic activity. The photocatalytic activity was evaluated for RhB dye degradation under UV-light irradiation (Fig. 6a and c). Fig. 6b and d show the plots of $\ln(C/C_0)$ vs. irradiation time. The reaction rate constants, k, are calculated by the kinetics Equation [44]:

$$\ln(C/C_0) = -kt, \quad (3)$$

Table 3
Comparison between the RhB degradation under UV light irradiation of SnO_2 particles synthesized in this work and those reported in the literature.

Sample	Method of synthesis	Catayst load (mg L^{-1})	RhB load (mol L^{-1})	Degradation efficiency/ duration	First order rate constant, k (min^{-1})	Ref.
SnO_2	Co-precipitation method	1000	$1\ 10^{-3}$	100%/10 min	0.3708	our work
SnO_2	Co-precipitation method and PAHT	1000	$1\ 10^{-3}$	100%/25 min	0.1626	our work
SnO_2	Co-precipitation method and calcinated 400°/1h	1000	$1\ 10^{-3}$	99.9%/60 min	0.06272	our work
SnO_2	Co-precipitation method, calcinated 400°/1 h and PAHT	1000	$1\ 10^{-3}$	100%/30 min	0.1192	our work
SnO_2	Precipitation method followed by sonication	1000	$5\ 10^{-5}$	51%/100 min	$0.653\ 10^{-4}$	[14]
SnO_2 NPs	Green synthesis route and calcinated 600 °C/2h	83	$2\ 10^{-5}$	91.7%/190 min	$1.2\ 10^{-2}$	[15]
SnO_2 NPs	Microwave-assisted hydrothermal method and calcinated 550 °C/2h	500	$2\ 10^{-5}$	5%/240 min	almost zero	[16]
SnO_2 QDs	Biosynthesis and calcinated 400 °C/2h	500	$8\ 10^{-5}$	70%/180 min	0.0069	[17]
SnO_2 NPs	Co-precipitation method and calcinated 600 °C/4h	1000	not informed	70%/90 min	not calculated	[18]
SnO_2	Hydrothermal method	80	$2\ 10^{-5}$	70%/80 min	$1.217\ 10^{-2}$	[19]

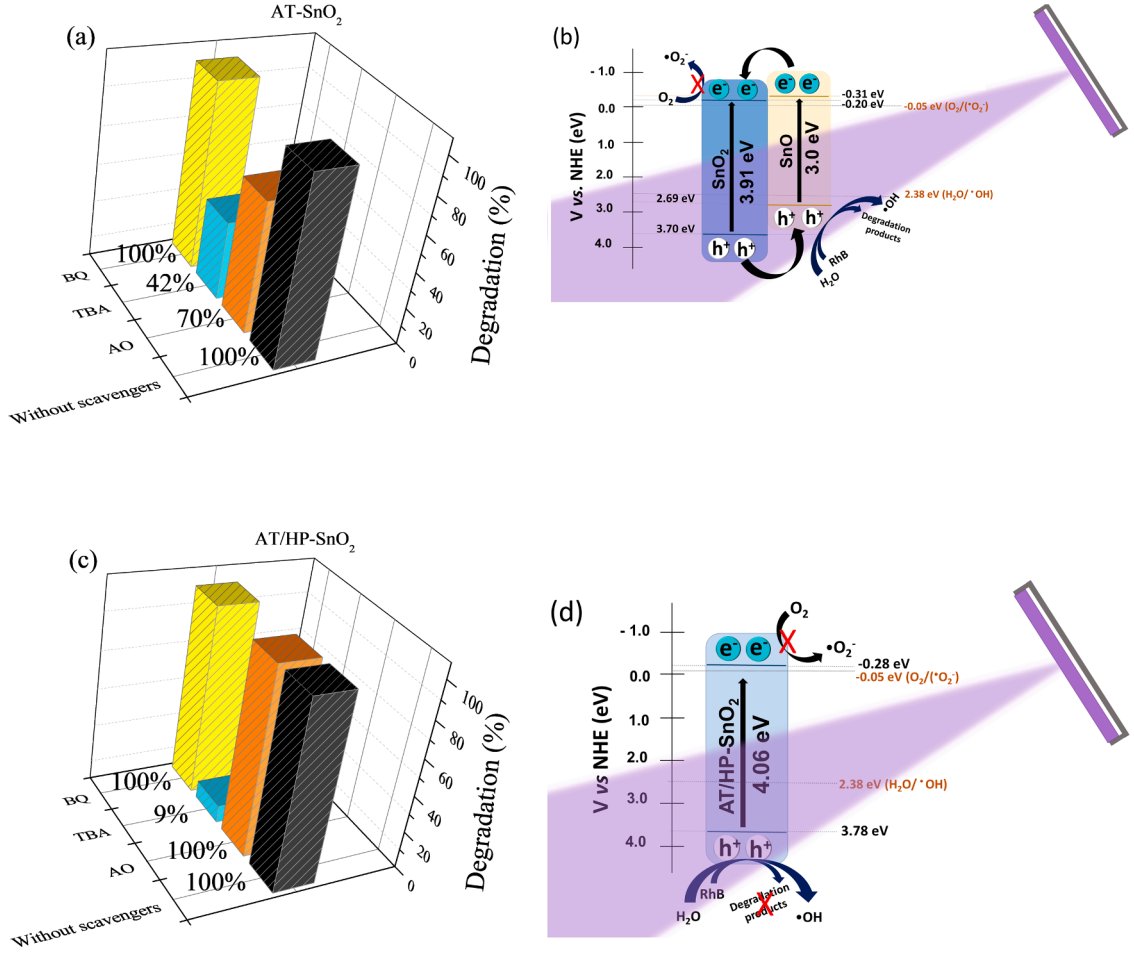

Fig. 7. Photodegradation of RhB using SnO_2 photocatalyst at ambient temperature under ambient pressure (a) and pressure-assisted heat treatment (c) with different quenchers, and possible UV-light-driven photocatalytic mechanism (b and d).

where k is the apparent pseudo-first-order rate constant, C_0 is the RhB concentration at the initial time, C is the dye concentration and t is the reaction time (min).

As shown in Fig. 6a and c, the self-degradation of pure RhB dye under UV-light irradiation is 30%. In Fig. 6a, it is possible to see the RhB degradation performance of the AT-SnO_2, 400 °C-SnO_2 and 700 °C-SnO_2 samples at ambient pressure. The AT-SnO_2 sample exhibits a higher photocatalytic activity than the others, probably due to the increased separation efficiency of electron–hole pairs. The increase in the calcination temperature (400 °C or 700 °C) leads to a reduced photocatalytic activity. These data are in agreement with the FE-SEM and PL results (Figs. 3 and 5a), where it is possible note that an increase in the calcination temperature results in an increase in the particle size and PL intensity, which in turn worsens the electron-hole charge separation rate [45]. However, when the samples are submitted a pressure-assisted heat treatment (Fig. 6c), there is a change in the photocatalytic activity in comparison with the samples synthesized at ambient pressure, evidencing the best photocatalytic activity for the AT-SnO_2 sample, whose irradiation time for the complete dye degradation increases by 15 min, while the time for complete dye degradation for the samples calcined at 400 and 700 °C is reduced by 30 and 35 min, respectively. According to Fig. 6e, the *k* value for AT-SnO_2 reduces about 43% when this sample is subjected to PAHT. On the other hand, the samples calcined at 400 and 700 °C (400 °C/HP-SnO_2 and 700 °C/HP-SnO_2) show an increase of approximately 190% in the reaction rate constant when submitted to pressure-assisted heat treatment.

The E_g value (Fig. 4) and the results obtained by PL (Fig. 5) indicate that the 400 °C/HP-SnO_2 sample has a better electron-hole separation, which would indicate an enhanced photodegradation performance. However, it can be observed that the AT/HP-SnO_2 sample, which was not previously calcined, exhibits higher performance when subjected to PAHT (Fig. 6c). One possible explanation for this behavior is the morphology of the samples, which influences the penetration of photons of light [46]. The cycle stability in the RhB solution of the AT-SnO_2 and 400 °C/HP-SnO_2 samples, Fig. S2 (SI), reveal that after three cycles of dye degradation, both samples are stable.

Table 3 shows the photocatalytic efficiency of SnO_2 synthesized by our group in comparison with others in the literature. The data presented in Table 3 indicate that the synthesis of SnO_2 particles by the co-precipitation method at ambient temperature leads to a greater degradation efficiency of RhB under UV irradiation in a shorter time. The superior result was obtained by our group with 100% of dye degradation in only 10 min for the nanoparticle obtained at ambient temperature, which may be justified by the presence of the SnO secondary phase observed in the XRD analysis. Additionally, for the calcined sample subjected to PAHT, the dye degradation efficiency of RhB reaches 100% in just 30 min, being 3 times shorter and 30% more efficient than that obtained by the synthesized SnO_2 nanoparticles (NPs) by the same method. It can be seen that the RhB concentration used in our work is about 100 times higher than that used in the other mentioned works, but the catalyst load varies from 83 to 1000 mg L^{-1}.These results indicate that this method combined with our synthesis conditions lead to the formation of SnO_2 with improved dye degradation efficiency under UV irradiation.

A series of radical trapping experiments were performed using tert-butyl alcohol (TBA), ammonium oxalate (AO) and benzoquinone (BQ)

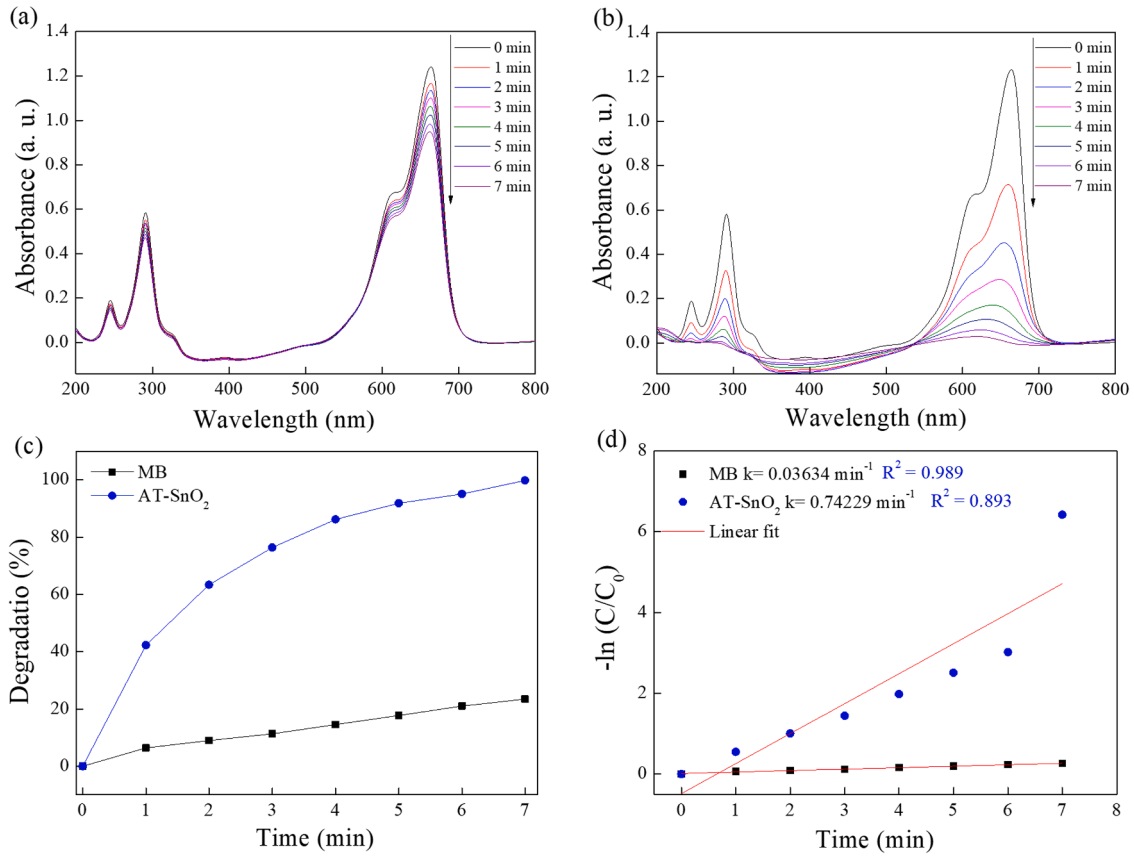

Fig. 8. Photodegradation of pure MB (a) and MB with AT-SnO_2 sample (b) under UV irradiation at 664 nm, degradation percentage with time (c) and rate constant value of the photocatalytic degradation with the respective linear regression coefficient (R^2) (d).

scavengers to propose a possible photocatalytic mechanism. BQ, AO and TBA were added to quencher the presence of superoxide radical anions ($O_2^{\cdot-}$), hole (h^+) and hydroxyl radicals (·OH), respectively [47]. Fig. 7a shows the photocatalytic activity of AT-SnO_2 sample in the presence of these quenchers. It is possible to note that the addition of BQ has no effect on the RhB degradation, indicating that the $O_2^{\cdot-}$ radical does not participate in the degradation mechanism. On the other hand, the addition of both TBA and AO results in a suppression of the degradation rate. Therefore, the results reveal that the ·OH radicals are the main reactive species during the photocatalytic oxidation of RhB, followed by h^+. When this sample is subjected to pressure-assisted heat treatment (Fig. 7c), the ·OH radicals are the only reactive species during the photocatalytic oxidation of RhB. In contrast, the result obtained for the 400 °C-SnO_2 sample (Fig. S3a, SI) demonstrates that h^+ does not participate in the dye degradation mechanism, while the ·OH radicals are the dominant species in the mechanism, followed to a lesser extent by the $O_2^{\cdot-}$ radical. When this sample is subjected to PAHT (400 °C/HP-SnO_2) (Fig. S3c, SI), the ·OH radicals are the reactive species during the photocatalytic oxidation of RhB, followed to a lesser extent by the h^+ and the $O_2^{\cdot-}$ radical.

The possible photocatalytic mechanism for the SnO_2 samples under UV light is shown in Figs. 7(b,d) and S3(b,d). The valence band (VB) and the conduction band (CB) potentials (E_{VB} and E_{CB}, respectively) can be calculated by Mulliken electronegativity theory using the derived empirical Equations [48]:

$$E_{VB} = \chi - E_e + 0.5E_g, \quad (4)$$

$$E_{CB} = E_{VB} - E_g, \quad (5)$$

where χ is the electronegativity of the semiconductor, E_e is the free electron energy on the hydrogen scale (4.5 eV) and E_g is the band gap energy. It is important to mention that the SnO_2 electronegativity is 6.25 eV [49]. The high photocatalytic RhB degradation by the AT-SnO_2 sample can be explained by the existence of the SnO second phase that can provides an improved charge carrier separation, so less electron–hole (e^--h^+) pairs recombination occurs since the charge carriers are separated on different materials structures, SnO_2-SnO. However, it was not possible to observe the presence of the SnO band gap together with the AT-SnO_2 band gap (Fig. 4a). Thus a band diagram with the charge separation of the SnO_2–SnO (n-type semiconductor–p-type semiconductor) is proposed using the band gap value for the SnO reported in the literature (3.0 eV) [50], and electronegativity of 5.69 eV [51], Fig. 7b. When AT-SnO_2 photocatalyst was excited by UV light with higher energy than its band gap, the e^--h^+ pairs are generated. The photogenerated e^- transfer could occurs from the CB of SnO (−0.31 eV) to the CB of SnO_2 (−0.20 eV). In the meantime, the photogenerated h^+ transfer can take place from the VB of SnO_2 (3.70 eV) to the VB of SnO (2.69 eV), suggesting that the photogenerated e^- and h^+ were efficiently separated. The h^+ acts as an oxidizing agent and oxidizes either the RhB dye directly or water to form ·OH radicals ($E^\circ_{\cdot OH/OH} = 2.38$ eV *vs.* NHE). The quenching experiments (Fig. 7a) indicate that the photodegradation by $O_2^{\cdot-}$ radicals does not occur even though it has a more negative potential ($E_{CB} = -0.20$ eV *vs.* NHE) than O_2/ $O_2^{\cdot-}$ ($E^\circ_{O2/O2\cdot-} = -0.05$ eV *vs.* NHE) [52]. On the other hand, when the AT-SnO_2 sample subjected to pressure treatment (AT/HP-SnO_2) was excited by UV light, e^- from the VB are transferred to the CB and as a result the e^-- h^+ pairs are formed (Fig. 7d). As indicated by the quenching experiments (Fig. 7c), the h^+ acts as an oxidizing agent, forming only hydroxyl radical (·OH) by reaction with H_2O. The ·OH radical participated in the RhB degradation process, being absorbed on the surface of SnO_2 photocatalyst [53].

The reduced photodegradation activity of the sample submitted to pressure treatment (AT/HP-SnO_2) when compared to the sample

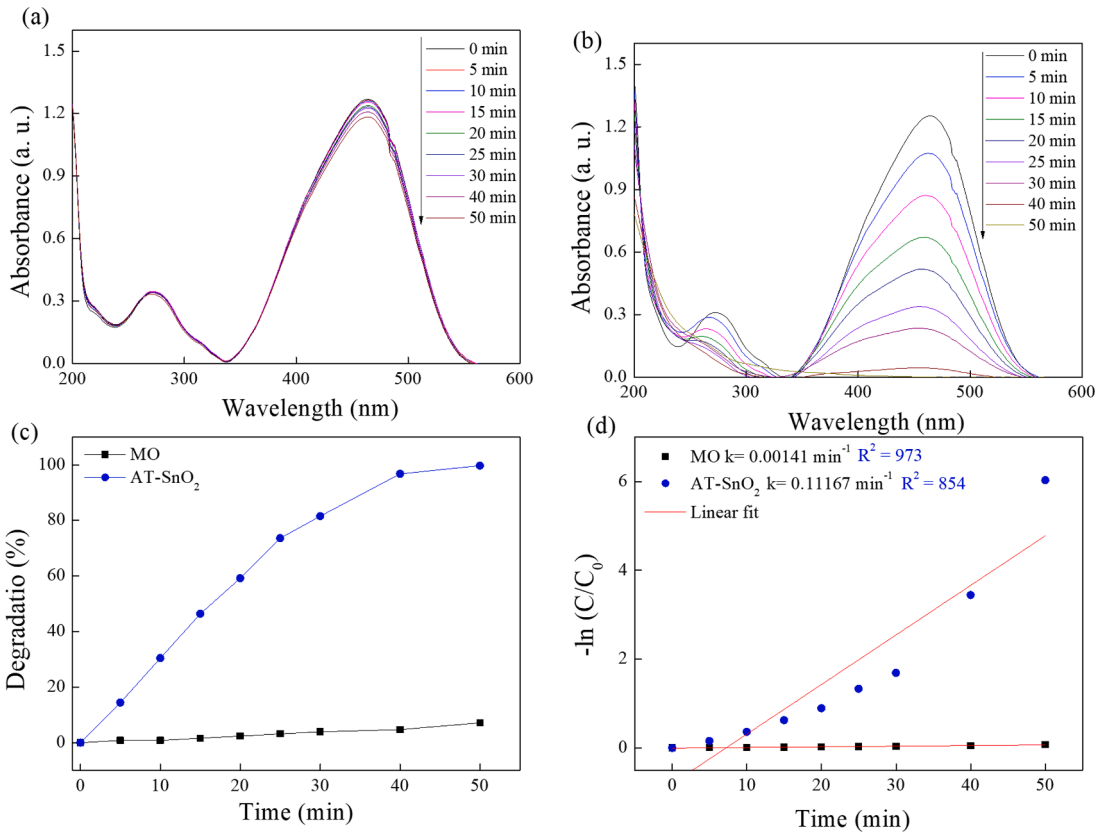

Fig. 9. Photodegradation of pure MO (a) and MO with AT-SnO_2 sample (b) under UV irradiation at 464 nm, degradation percentage with time (c) and rate constant value of photocatalytic degradation with the respective linear regression coefficient (R^2) (d).

without pressure treatment (AT-SnO_2) can be explain by two reasons. First, the presence of the SnO phase in the AT-SnO_2 sample that provides an improved charge carrier separation. Second, the fact that the only mechanism for the RhB dye degradation in the AT/HP-SnO_2 sample is through ·OH radicals, which have a slow combination time with the h^+ and the OH^- (10^{-3} s), restricting the increased SnO_2 photodegradation activities [54].

Fig. S3b(SI) presents the possible mechanism for the 400 °C-SnO_2 sample. Based on the results of photodegradation with different scavengers, the mechanism for the RhB dye degradation is exclusively by ·OH radicals. When this sample is subjected to pressure treatment (400 °C/HP- SnO_2) (Fig. S3d, SI), the dye is degraded mainly by the ·OH radicals and to a lesser extent by the O_2^{-} radicals and the h^+. The explanation for the 190% improvement of the reaction rate constant (Fig. 6e) when the sample is subjected to pressure-assisted heat treatment lies in the fact that the main mechanism for the RhB degradation at ambient pressure is by ·OH radicals, which have a slow combination time with the h^+, thus making the rate constant slow. When this sample undergoes pressure treatment, the rate constant increases due to the presence of the three photodegradation mechanisms.

The superior result regarding the best photocatalytic activity for RhB degradation reached by the AT-SnO_2 sample in comparison with those submitted to temperature and pressure treatments and the results obtained in the literature (Table 3) led us to investigate its performance for the degradation of other dyes, such as methylene blue (MB) and methyl orange (MO).

The photocatalytic degradation of the MB solution (1 10^{-3} mol L^{-1}) was studied using 50 mg of the AT-SnO_2 sample, as shown in Fig. 8. It

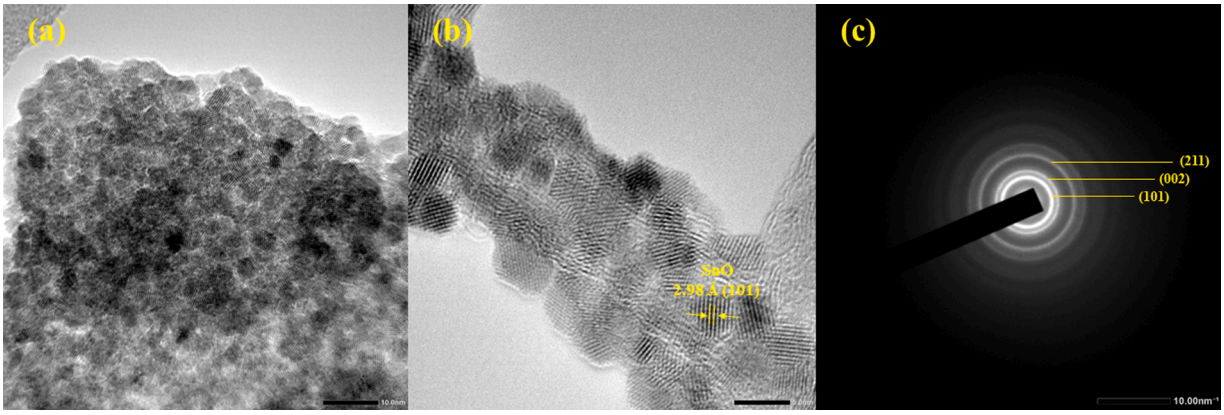

Fig. 10. TEM image (a), HRTEM image (b) and SAED pattern of spherical nanoparticles in AT-SnO_2 sample.

Table 4
Specific surface area, pore volume and pore size of SnO_2 and SnO_2 samples calcinated at different temperatures and under ambient pressure.

Sample	BET specific surface area (m^2 g^{-1})	Pore volume (cm^3 g^{-1})	Pore size (nm)
AT-SnO_2	194.13	0.1067	2.20
400 °C-SnO_2	43.55	0.0399	3.67
700 °C-SnO_2	21.30	0.0481	9.03

can be seen that when the catalyst is added to the dye, the characteristic peaks of the MB are significantly reduced under UV irradiation in 7 min (Fig. 8a and b). Fig. 8c shows that the degradation efficiency reaches 100% in 7 min. Fig. 8d indicates that the photodegradation of the MB solution with the AT-SnO_2 sample follows pseudo-first-order kinetics with a higher rate constant ($k = 0.74229$ min^{-1}), causing this sample to have a higher photocatalytic activity. The photocatalytic activity of AT-SnO_2 in the presence of quenchers, Fig. S4a (SI), reveal that the ·OH radicals are the main reactive species during the photocatalytic oxidation of MB dye, followed by $h^+$and $O_2^{\cdot-}$ radicals. By comparing our results to those obtained by Kim et al. [55] for the SnO_2 sample obtained by precipitation method and calcinated at 380 °C for 2 h, we found that our AT-SnO_2 sample has a superior performance for MB degradation under UV light irradiation, as the calcinated SnO_2 sample degraded 79% of the dye in 180 min.

The photocatalytic degradation of the MO solution (1 10^{-3} mol L^{-1}) was studied using 50 mg of the AT-SnO_2 sample. Fig. 9 shows that the addition of the catalyst to the dye solution causes the absorbance of the characteristic peaks of MO to be significantly reduced when this solution is irradiated by UV light for 50 min (Fig. 9a and b). Fig. 9c reveals that the degradation efficiency reaches 100% in 50 min. Fig. 9d indicates that the dye photodegradation with the AT-SnO_2 sample follows pseudo-first-order kinetics with a k value of 0.11167 min^{-1}. The photocatalytic activity of AT-SnO_2 in the presence of quenchers, Fig. S4c (SI), reveal that the $O_2^{\cdot-}$ radicals are the main reactive species during the photocatalytic oxidation of MO dye, followed by ·OH and h^+.

The results demonstrate that the AT-SnO_2 sample is highly efficient for the removal of cationic dyes (RhB and MB) when irradiated by UV light. Regarding the anionic dye MO, the degradation efficiency obtained is 39% greater than that found in the literature (61%) over a longer period of time (100 min) [14].

The morphology of the AT-SnO_2 sample plays a dynamic part in the increase of the photocatalytic degradation rate. To confirm its dimension, morphology, and microstructure, the TEM analyses were used to provide precise research. Fig. 10a displays the TEM image of a region of the AT-SnO_2 sample, where it is possible to note an agglomerate of spherical particles. Despite the fact that the particle size distribution is unreliable due to its agglomeration, it can be clearly observed that the particles present diameters much smaller than 10 nm. According to the HRTEM image and the fast Fourier transform (FFT) analysis (Fig. 10b), these nanoparticles are composed of SnO tetragonal phase (ICSD 15516) with P4/nmm space group [56]. To further confirm the SnO phase, a selected area electron diffraction (SAED) measurement was performed in a particular region composed of these nanoparticles (Fig. 10c). The results indicate polycrystallinity of this sample region caused by small particle sizes, resulting in random orientation and confirming the SnO phase by the presence of its (101), (002) and (211) crystalline planes with interplanar distances of 2.98 Å, 2.40 Å, and 1.59 Å, respectively. Only the SnO phase was observed in the TEM analysis due to the technique limitation in measuring small particle sizes. Therefore, according to the main presence of SnO_2 phase in the AT-SnO_2 sample, as observed by the XRD and Raman analyses, it can be concluded that this sample is composed of SnO nanoparticles dispersed in the SnO_2 microparticles, as seen in the FE-SEM images. Therefore, the remarkable high photocatalytic activity of the AT-SnO_2 sample can be assigned to the formation of two-phase material consisting of SnO_2 and SnO. Probably the SnO second phase separates the charge carriers generated upon UV irradiation efficiently, thereby thus decreasing the recombination rate of e^-- h^+ pairs and thus improving the ·OH radical generation.

BET surface area values, pore volume and pore size of the AT-SnO_2, 400 °C-SnO_2 and 700 °C-SnO_2 samples are listed in Table 4. The specific surface area value of the AT-SnO_2 sample (194.13 m^2 g^{-1}) induces superior photocatalytic degradation rate due to its large surface area when compared to the calcinated samples. This large surface area causes high redox reaction to create more electron-hole pairs, which participate in the photocatalytic reaction and help to reach superior degradation rate [57].

The FE-SEM, TEM, and BET characterization results show that the photocatalytic activity of the AT-SnO_2 sample has superior degradation rate due to the existence of the SnO second phase, the synthesis conditions, and mainly its high specific surface area.

4. Conclusion

SnO_2 samples were prepared by the co-precipitation method and submitted to different calcination temperature and pressure-assisted heat treatment (PAHT). The XRD characterization showed that all samples presented the formation of the SnO phase. The performance of the samples as photocatalysts for RhB degradation under UV irradiation followed the dye degradation order: 700 °C/HP-SnO_2 < 400 °C/HP-SnO_2 < AT/HP-SnO_2 < AT-SnO_2. This result demonstrated that PAHT improved the performance of the samples calcined at different temperatures, and negatively interfered with the performance of the sample without previous heat treatment. In addition, the synthesized AT-SnO_2 was also tested for the degradation of MB and MO dyes. The results revealed that this sample reached a superior performance in the degradation of RhB, MB and MO in comparison with the results presented in the literature. This excellent performance was attributed to the to the existence of the SnO second phase, the synthesis conditions, and mainly its high specific surface area. It can then be concluded that the synthesized AT-SnO_2 is promising for photocatalytic applications regarding the degradation of anionic and cationic dyes under UV irradiation.

Declaration of Competing Interest

The authors declare that they have no known competing financial interests or personal relationships that could have appeared to influence the work reported in this paper.

Acknowledgments

The authors appreciate the support of the Brazilian research financing institutions: Conselho Nacional de Desenvolvimento Científico e Tecnológico- CNPq (163342/2020-2), São Paulo Research Foundation – FAPESP (2013/07296-2) and Coordenação de Aperfeiçoamento de Pessoal de Nível Superior - Brasil (CAPES) - Finance Code 001.

Supplementary materials

Supplementary material associated with this article can be found, in the online version, at doi:10.1016/j.materresbull.2022.111914.

References

[1] D. Kaur, V. Bagga, N. Behera, B. Thakral, A. Asija, J. Kaur, S. Kaur, SnSe/SnO_2 nanocomposites: novel material for photocatalytic degradation of industrial waste dyes, Adv. Compos. Hybrid Mater. 2 (2019) 763–776, https://doi.org/10.1007/s42114-019-00130-7.
[2] S.K. Tammina, B.K. Mandal, N.K. Kadiyala, Photocatalytic degradation of methylene blue dye by nonconventional synthesized SnO_2 nanoparticles, Environ.

Nanotechnol. Monit. Manag. 10 (2018) 339–350, https://doi.org/10.1016/j.enmm.2018.07.006.
[3] A.M. Al-Hamdi, M. Sillanpää, J. Dutta, Photocatalytic degradation of phenol by iodine doped tin oxide nanoparticles under UV and sunlight irradiation, J. Alloy. Compd. 618 (2015) 366–371, https://doi.org/10.1016/j.jallcom.2014.08.120.
[4] D. Mohanta, K. Barman, Sk. Jasimuddin, Md. Ahmaruzzaman, MnO doped SnO_2 nanocatalysts: activation of wide band gap semiconducting nanomaterials towards visible light induced photoelectrocatalytic water oxidation, J. Colloid Interface Sci. 505 (2017) 756–762, https://doi.org/10.1016/j.jcis.2017.06.064.
[5] P.G. Choi, N. Izu, N. Shirahata, Y. Masuda, Improvement of sensing properties for SnO_2 gas sensor by tuning of exposed crystal face, Sens. Actuators B Chem. 296 (2019), 126655, https://doi.org/10.1016/j.snb.2019.126655.
[6] M.M. Shahraki, S. Alipour, P. Mahmoudi, A. Karimi, Novel multifunctional capacitor-varistor ceramics based on SnO_2, Ceram. Int. 44 (2018) 20386–20390, https://doi.org/10.1016/j.ceramint.2018.08.031.
[7] A.J. Singh, T. Jahnke, Y. Xiao, S. Wang, Y. Yu, H. David, G. Richter, P. Laux, A. Luch, A. Srivastava, P.S. Saxena, J. Bill, M. Sitti, Peptide-induced biomineralization of tin oxide (SnO_2) nanoparticles for antibacterial applications, J. Nanosci. Nanotechnol 19 (2019) 5674–5686, https://doi.org/10.1166/jnn.2019.16645.
[8] L. Kavan, Z.V. Zivcova, M. Zlamalova, S.M. Zakeeruddin, M. Grätzel, Electron-selective layers for dye-sensitized solar cells based on TiO_2 and SnO_2, J. Phys. Chem. C 124 (2020) 6512–6521, https://doi.org/10.1021/acs.jpcc.9b11883.
[9] M. Batzill, Fundamental aspects of surface engineering of transition metal oxide photocatalysts, Energy Environ. Sci. 4 (2011) 3275–3286, https://doi.org/10.1039/C1EE01577J.
[10] J. Wang, H. Fan, H. Yu, Synthesis of hierarchical porous Zn-doped SnO_2 spheres and their photocatalytic properties, J. Mater. Eng. Perform. 24 (2015) 4260–4266, https://doi.org/10.1007/s11665-015-1745-1.
[11] P. Manjula, R. Boppella, S.V. Manorama, A facile and green approach for the controlled synthesis of porous SnO_2 nanospheres: application as an efficient photocatalyst and an excellent gas sensing material, ACS Appl. Mater. Interfaces 4 (2012) 6252–6260, https://doi.org/10.1021/am301840s.
[12] A. Sadeghzadeh-Attar, Efficient photocatalytic degradation of methylene blue dye by SnO_2 nanotubes synthesized at different calcination temperatures, Sol. Energy Mater. Sol. Cells 183 (2018) 16–24, https://doi.org/10.1016/j.solmat.2018.03.046.
[13] Y. Li, Q. Yang, Z. Wang, G. Wang, B. Zhang, Q. Zhang, D. Yang, Rapid fabrication of SnO_2 nanoparticle photocatalyst: computational understanding and photocatalytic degradation of organic dye, Inorg. Chem. Front. 5 (2018) 3005–3014, https://doi.org/10.1039/C8QI00688A.
[14] V.K. Gupta, R. Saravanan, S. Agarwal, F. Gracia, M.M. Khan, J. Qin, R. V. Mangalaraja, Degradation of azo dyes under different wavelengths of UV light with chitosan-SnO_2 nanocomposites, J. Mol. Liq. 232 (2017) 423–430, https://doi.org/10.1016/j.molliq.2017.02.095.
[15] J. Ebrahimian, M. Mohsennia, M. Khayatkashani, Photocatalytic-degradation of organic dye and removal of heavy metal ions using synthesized SnO_2 nanoparticles by Vitex agnus-castus fruit via a green route, Mater. Lett. 263 (2020), 127255, https://doi.org/10.1016/j.matlet.2019.127255.
[16] X. Wang, Y. He, L. Xu, Y. Xia, R. Gang, SnO_2 particles as efficient photocatalysts for organic dye degradation grown *in-situ* on g-C_3N_4 nanosheets by microwave-assisted hydrothermal method, Mater. Sci. Semicond. Process. 121 (2021), 105298, https://doi.org/10.1016/j.mssp.2020.105298.
[17] I. Fatimah, I. Sahroni, O. Muraza, R. an Doong, One-pot biosynthesis of SnO_2 quantum dots mediated by Clitoria ternatea flower extract for photocatalytic degradation of Rhodamine B, J. Environ. Chem. Eng. 8 (2020), 103879, https://doi.org/10.1016/j.jece.2020.103879.
[18] H. Letifi, Y. Litaiem, D. Dridi, S. Ammar, R. Chtourou, Enhanced photocatalytic activity of vanadium-doped SnO_2 nanoparticles in Rhodamine B degradation, Adv. Condens. Matter Phys. 2019 (2019) 11, https://doi.org/10.1155/2019/2157428, pages.
[19] R. Shyamala, L.G. Devi, Reduced graphene oxide/SnO_2 nanocomposites for the photocatalytic degradation of Rhodamine B: preparation, characterization, photosensitization, vectorial charge transfer mechanism and identification of reaction intermediates, Chem. Phys. Lett. 748 (2020), 137385, https://doi.org/10.1016/j.cplett.2020.137385.
[20] S. Schmidt, E.T. Kubaski, D.P. Volanti, T. Sequinel, V.D.N. Bezzon, A. Beltrán, S. M. Tebcherani, J.A. Varela, Effect of pressure-assisted heat treatment on photoluminescence emission of α-Bi_2O_3 needles, Inorg. Chem. 54 (2015) 10184–10191, https://doi.org/10.1021/acs.inorgchem.5b01237.
[21] N. Rani, N. Jaggi, Effect of reaction temperature on the structural and electronic properties of stannic oxide nanostructures, Bull. Mater. Sci. 43 (2020) 146, https://doi.org/10.1007/s12034-020-02141-3.
[22] L. Li, C. Zhang, W. Chen, Fabrication of SnO_2–SnO nanocomposites with p–n heterojunctions for the low-temperature sensing of NO_2 gas, Nanoscale 7 (2015) 12133–12142, https://doi.org/10.1039/c5nr02334c.
[23] E.R. Leite, J.A. Cerri, E. Longo, J.A. Varela, C.A. Paskocima, Sintering of ultrafine undoped SnO_2 powder, J. Eur. Ceram. Soc. 21 (2001) 669–675, https://doi.org/10.1016/S0955-2219(00)00250-8.
[24] M. Suleiman, C. Borchers, M. Guerdane, N.M. Jisrawi, D. Fritsch, R. Kirchheim, A. Pundt, Size and structure of palladium clusters determined by XRD and HREM, Z. Phys. Chem. 233 (2009) 169–181, https://doi.org/10.1524/zpch.2009.6031.
[25] M. Aziz, S.S. Abbas, W.R.W. Baharom, Size-controlled synthesis of SnO_2 nanoparticles by sol–gel method, Mater. Lett. 91 (2013) 31–34, https://doi.org/10.1016/j.matlet.2012.09.079.
[26] J.A. Toledo-Antonio, R. Gutiérrez-Baez, P.J. Sebastian, A. Vázquez, Thermal stability and structural deformation of rutile SnO_2 nanoparticles, J. Solid State Chem. 174 (2003) 241–248, https://doi.org/10.1016/S0022-4596(03)00181-6.
[27] Z.W. Chen, J.K.L. Lai, C.H. Shek, Insights into microstructural evolution from nanocrystalline SnO_2 thin films prepared by pulsed laser deposition, Phys. Rev. B 70 (2004), 165314, https://doi.org/10.1103/PhysRevB.70.165314.
[28] S. Chacko, N.S. Philip, K.G. Gopchandran, P. Koshy, V.K. Vaidyan, Nanostructural and surface morphological evolution of chemically sprayed SnO_2 thin films, Appl. Surf. Sci. 254 (2008) 2179–2186, https://doi.org/10.1016/j.apsusc.2007.09.027.
[29] A. Sharma, D. Prakash, K.D. Verma, Optical characterization of hydrothermally grown SnO_2 nanocrystals, J. Optoelectron. Adv. Mater. 11 (2009) 331–337.
[30] Zulfiqar, R. Khan, Y. Yuan, Z. Iqbal, J. Yang, W. Wang, Z. Ye, J. Lu, Variation of structural, optical, dielectric and magnetic properties of SnO_2 nanoparticles, J. Mater. Sci. Mater.: Electron. 28 (2017) 4625–4636, https://doi.org/10.1007/s10854-016-6101-1.
[31] H.A. Gatea, Impact of sintering temperature on crystallite size and optical properties of SnO_2 nanoparticles, J. Phys. Conf. Ser. 1829 (2017), 012030, https://doi.org/10.1088/1742-6596/1829/1/012030.
[33] S. Pazouki, N. Memarian, Effects of hydrothermal temperature on the physical properties and anomalous band gap behavior of ultrafine SnO_2 nanoparticles, Optik 246 (2021), 167843, https://doi.org/10.1016/j.ijleo.2021.167843 (Stuttg.).
[32] X. Guan, Y. Wang, P. Luo, Y. Yu, D. Chen, X. Li, Incorporating N atoms into SnO_2 nanostructure as an approach to enhance gas sensing property for acetone, Nanomaterials 9 (2019) 445, https://doi.org/10.3390/nano9030445.
[34] X. Wang, X. Wang, Q. Di, H. Zhao, B. Liang, J. Yang, Mutual effects of fluorine dopant and oxygen vacancies on structural and luminescence characteristics of F doped SnO_2 nanoparticles, Materials 10 (2017) 1398, https://doi.org/10.3390/ma10121398 (Basel).
[35] T. Jia, J. Chen, Z. Deng, F. Fu, J. Zhao, X. Wang, F. Long, Facile synthesis of Zn-doped SnO_2 dendrite-built hierarchical cube-like architectures and their application in lithium storage, Mater. Sci. Eng. B 189 (2014) 32–37, https://doi.org/10.1016/j.mseb.2014.07.006.
[36] X. Liu, J. Iqbal, Z. Wu, B. He, R. Yu, Structure and room-temperature ferromagnetism of Zn-doped SnO_2 nanorods prepared by solvothermal method, J. Phys. Chem. C 114 (2010) 4790–4796, https://doi.org/10.1021/jp909178x.
[37] Y.Q. Guo, R.Q. Tan, X. Li, J.H. Zhao, Z.L. Luo, C. Gao, W.J. Song, Shape-controlled growth and single-crystal XRD study of submillimeter-sized single crystals of SnO, Cryst. Eng. Comm. 13 (2011) 5677–5680, https://doi.org/10.1039/C0CE00949K.
[38] P. Makuła, M. Pacia, W. Macyk, How to correctly determine the band gap energy of modified semiconductor photocatalysts based on UV–Vis spectra, J. Phys. Chem. Lett. 9 (2018) 6814–6817, https://doi.org/10.1021/acs.jpclett.8b02892.
[39] L.G. da Trindade, K.M.N. Borba, A.B. Trench, L. Zanchet, V. Teodoro, F.M. L. Pontes, E. Longo, T.M. Mazzo, Effective strategy to coupling Zr-MOF/ZnO: synthesis, morphology and photoelectrochemical properties evaluation, J. Solid State Chem. 293 (2021), 121794, https://doi.org/10.1016/j.jssc.2020.121794.
[40] M. Bhatnagar, V. Kaushik, A. Kaushal, M. Singh, B.R. Mehta, Structural and photoluminescence properties of tin oxide and tin oxide: C core–shell and alloy nanoparticles synthesised using gas phase technique, AIP Adv. 6 (2016), 095321, https://doi.org/10.1063/1.4964313.
[41] V.M. Aroutiounian, Metal oxide gas sensors decorated with carbon nanotubes, Lith. J. Phys. 55 (2015) 319, https://doi.org/10.3952/physics.v55i4.3230.
[42] J. Liqiang, Q. Yichun, W. Baiqi, L. Shudan, J. Baojiang, Y. Libin, F. Wei, F. Honggang, S. Jiazhong, Review of photoluminescence performance of nano-sized semiconductor materials and its relationships with photocatalytic activity, Sol. Energy Mater. Sol. Cells 90 (2006) 1773, https://doi.org/10.1016/j.solmat.2005.11.007.
[43] J.G. Yu, H.G. Yu, B. Cheng, X.J. Zhao, J.C. Yu, W.K. Ho, The effect of calcination temperature on the surface microstructure and photocatalytic activity of TiO_2 thin films prepared by liquid phase deposition, J. Phys. Chem. B 107 (2003) 13871, https://doi.org/10.1021/jp036158y.
[44] A.B. Trench, T.R. Machado, A.F. Gouveia, C.C. Foggi, V. Teodoro, I. Sánchez-Montes, M.M. Teixeira, L.G. da Trindade, N. Jacomaci, A. Perrin, C. Perrin, J. M. Aquino, J. Andrés, E. Longo, Rational design of W-doped Ag_3PO_4 as an efficient antibacterial agent and photocatalyst for organic pollutant degradation, ACS Omega 5 (2020) 23808–23821, https://doi.org/10.1021/acsomega.0c03019.
[45] B. Babu, A.N. Kadam, G.T. Rao, S.W. Lee, C. Byon, J. Shim, Enhancement of visible-light-driven photoresponse of Mn-doped SnO_2 quantum dots obtained by rapid and energy efficient synthesis, J. Lumin. 195 (2018) 283–289, https://doi.org/10.1016/j.jlumin.2017.11.040.
[46] V. Ramasubbu, P.R. Kumar, E.M. Mothi, K. Karuppasamy, H.S. Kim, T. Maiyalagan, X.S. Shajan, Highly interconnected porous TiO_2-Ni-MOF composite aerogel photoanodes for high power conversion efficiency in quasi-solid dye-sensitized solar cells, Appl. Surf. Sci. 496 (2019), 143646, https://doi.org/10.1016/j.apsusc.2019.143646.
[47] L.G. da Trindade, L. Zanchet, A.B. Trench, J.C. Souza, M.H. Carvalho, A.J.A. de Oliveira, E.C. Pereira, T.M. Mazzo, E. Longo, Flower-like ZnO/ionic liquid composites: structure, morphology, and photocatalytic activity, Ionics 25 (2019) 3197–3210, https://doi.org/10.1007/s11581-018-2822-x (Kiel).
[48] M. Kandasamy, A. Seetharaman, D. Sivasubramanian, A. Nithya, K. Jothivenkatachalam, N. Maheswari, M. Gopalan, S. Dillibabu, A. Eftekhari, Ni-doped SnO_2 nanoparticles for sensing and photocatalysis, ACS Appl. Nano Mater. 1 (2018) 5823–5836, https://doi.org/10.1021/acsanm.8b01473.
[49] E. Abdelkader, L. Nadjia, B. Ahmed, Preparation and characterization of novel $CuBi_2O_4$/SnO_2 p–n heterojunction with enhanced photocatalytic performance under UVA light irradiation, J. King Saud Univ. Sci. 27 (2015) 76–91, https://doi.org/10.1016/j.jksus.2014.06.002.

[50] Q. Yan, J. Wang, X. Han, Z. Liu, Soft-chemical method for fabrication of SnO–TiO_2 nanocomposites with enhanced photocatalytic activity, J. Mater. Res. 28 (2013) 1862–1869, https://doi.org/10.1557/jmr.2013.135.
[51] Y. Xu, M.A.A. Schoonen, The absolute energy positions of conduction and valence bands of selected semiconducting minerals, Am. Mineral. 85 (2000) 543–556, https://doi.org/10.2138/am-2000-0416.
[52] S.P. Kim, M.Y. Choi, H.C. Choi, Photocatalytic activity of SnO_2 nanoparticles in methylene blue degradation, Mater. Res. Bull. 74 (2016) 85–89, https://doi.org/10.1016/j.materresbull.2015.10.024.
[53] A. Mohammadzadeh, M. Khoshghadam-Pireyousefan, B. Shokrianfard-Ravasjan, M. Azadbeh, H. Rashedi, M. Dibazar, A. Mostafaei, Synergetic photocatalytic effect of high purity ZnO pod shaped nanostructures with H_2O_2 on methylene blue dye degradation, J. Alloy. Compd. 845 (2020), 156333, https://doi.org/10.1016/j.jallcom.2020.156333.
[54] J.S. Romão, M.S. Hamdy, G. Mul, J. Baltrusaitis, Photocatalytic decomposition of cortisone acetate in aqueous solution, J. Hazard. Mater. 282 (2015) 208–215, https://doi.org/10.1016/j.jhazmat.2014.05.087.
[55] S.P. Kim, M.Y. Choi, H.C. Choi, Photocatalytic activity of SnO_2 nanoparticles in methylene blue degradation, Mater. Res. Bull. 74 (2016) 85–89, https://doi.org/10.1016/j.materresbull.2015.10.024.
[56] F. Izumi, Pattern-fitting structure refinement of tin (II) oxide, J. Solid State Chem. 38 (1981) 381–385, https://doi.org/10.1016/0022-4596(81)90068-2.
[57] L. Gnanasekaran, R. Hemamalini, R. Saravanan, K. Ravichandran, F. Gracia, S. Agarwal, V.K. Gupta, Synthesis and characterization of metal oxides (CeO_2, CuO, NiO, Mn_3O_4, SnO_2 and ZnO) nanoparticles as photo catalysts for degradation of textile dyes, J. Photochem. Photobiol. B 173 (2017) 43–49, https://doi.org/10.1016/j.jphotobiol.2017.05.027.